A two-lane mechanism for selective biological ammonium transport

Gordon Williamson[1†], Giulia Tamburrino[2,3†], Adriana Bizior[1†],
Mélanie Boeckstaens[4†], Gaëtan Dias Mirandela[1‡], Marcus G Bage[2,3],
Andrei Pisliakov[2,3], Callum M Ives[2], Eilidh Terras[1], Paul A Hoskisson[1],
Anna Maria Marini[4], Ulrich Zachariae[2,3*], Arnaud Javelle[1*]

[1]Strathclyde Institute of Pharmacy and Biomedical Sciences, University of
Strathclyde, Glasgow, United Kingdom; [2]Computational Biology, School of Life
Sciences, University of Dundee, Dundee, United Kingdom; [3]Physics, School of
Science and Engineering, University of Dundee, Dundee, United Kingdom; [4]Biology
of Membrane Transport Laboratory, Department of Molecular Biology, Université
Libre de Bruxelles, Gosselies, Belgium

*For correspondence:
u.zachariae@dundee.ac.uk (UZ);
arnaud.javelle@strath.ac.uk (AJ)

[†]These authors contributed
equally to this work

Present address: [‡]Wellcome
Trust Centre for Cell Biology,
Michael Swann Building, The
King's Buildings, University of
Edinburgh, Edinburgh, United
Kingdom

Abstract The transport of charged molecules across biological membranes faces the dual
problem of accommodating charges in a highly hydrophobic environment while maintaining
selective substrate translocation. This has been the subject of a particular controversy for the
exchange of ammonium across cellular membranes, an essential process in all domains of life.
Ammonium transport is mediated by the ubiquitous Amt/Mep/Rh transporters that includes the
human Rhesus factors. Here, using a combination of electrophysiology, yeast functional
complementation and extended molecular dynamics simulations, we reveal a unique two-lane
pathway for electrogenic NH_4^+ transport in two archetypal members of the family, the transporters
AmtB from *Escherichia coli* and Rh50 from *Nitrosomonas europaea*. The pathway underpins a
mechanism by which charged H^+ and neutral NH_3 are carried separately across the membrane after
NH_4^+ deprotonation. This mechanism defines a new principle of achieving transport selectivity
against competing ions in a biological transport process.

Introduction

The transport of ammonium across cell membranes is a fundamental biological process in all
domains of life. Ammonium exchange is mediated by the ubiquitous ammonium transporter/methyl-
ammonium-ammonium permease/Rhesus (Amt/Mep/Rh) protein family. The major role of bacterial,
fungal, and plant Amt/Mep proteins is to scavenge ammonium for biosynthetic assimilation, whereas
mammals are thought to produce Rh proteins in erythrocytes, kidney, and liver cells for detoxifica-
tion purposes and to maintain pH homeostasis (*Biver et al., 2008*; *Huang and Ye, 2010*). In humans,
Rh mutations are linked to pathologies that include inherited hemolytic anemia, stomatocytosis, and
early-onset depressive disorder (*Huang and Ye, 2010*). Despite this key general and biomedical
importance, so far, no consensus on the pathway and mechanism of biological ammonium transport
has been reached.

High-resolution structures available for several Amt, Mep and Rh proteins show a strongly hydro-
phobic pore leading towards the cytoplasm (*Andrade et al., 2005*; *Gruswitz et al., 2010*;
Khademi et al., 2004; *Lupo et al., 2007*; *van den Berg et al., 2016*). This observation led to the
conclusion that the species translocated through Amt/Mep/Rh proteins is neutral NH_3. However, this
view has been experimentally challenged, first for some plant Amt proteins (*Ludewig et al., 2002*;
Mayer et al., 2006; *McDonald and Ward, 2016*; *Neuhäuser et al., 2014*), followed by further *in-
vitro* studies revealing that the activity of bacterial Amt proteins is electrogenic (*Mirandela et al.,*

2019; Wacker et al., 2014). Taken together, these findings renewed a long-standing debate on the mechanism by which a charged molecule is translocated through a hydrophobic pore and how selectivity for NH_4^+ over competing ions is achieved.

Here, we reveal the pathways, mechanism, and key determinants of selectivity of electrogenic ammonium transport in Amt and Rh proteins, unifying the diverse observations that led to these seemingly incompatible suggestions. The transport mechanism is underpinned by the separate transfer of H^+ and NH_3 on a unique two-lane pathway following NH_4^+ sequestration and deprotonation. This mechanism ensures that ammonium – which occurs mainly in protonated form in the aqueous phase – is efficiently translocated across the membrane, while maintaining strict selectivity against K^+, a monovalent cation of similar size. This previously unobserved principle is likely to form a new paradigm for the electrogenic members of the Amt/Mep/Rh family. Similar mechanisms may be utilized by other membrane transporters to facilitate the selective translocation of pH-sensitive molecules.

Results and discussion

AmtB and NeRh50 activity is electrogenic

Motivated by our finding that the activity of *Escherichia coli* AmtB is electrogenic (*Mirandela et al., 2019*), we first investigated the transport mechanism of the Rh50 protein from *Nitrosomonas europaea* (NeRh50). Rh and Amt proteins are distant homologs, and thus a functional distinction between both subfamilies has been proposed (*Huang and Ye, 2010*). The architecture of NeRh50 is highly representative of Rh proteins (*Gruswitz et al., 2010*; *Lupo et al., 2007*) which have been repeatedly reported to serve as electroneutral NH_3 or CO_2 gas channels (*Cherif-Zahar et al., 2007*; *Hub et al., 2010a*; *Li et al., 2007*; *Lupo et al., 2007*; *Weidinger et al., 2007*). The activity of purified NeRh50 reconstituted into liposomes was quantified using Solid-Supported Membrane Electrophysiology (SSME) (*Bazzone et al., 2017*) experiments, where we recorded a NH_4^+-selective current (*Figure 1*) with a decay rate that is strongly dependent on the lipid-to-protein ratio (LPR; *Table 1*, *Figure 1— figure supplement 1*). Expressed in a *Saccharomyces cerevisiae* triple-mepΔ strain, deprived of its three endogenous Mep ammonium transporters, NeRh50 complemented the growth defect on minimal medium containing ammonium as sole nitrogen source (*Figure 1*). The electrogenic transport activity observed for NeRh50 and AmtB may suggest a common transport mechanism amongst the distant Amt and Rh proteins, but more experiments are needed to conclusively confirm this. Also, the NH_4^+ selectivity of both transporters further highlighted the question of how these proteins achieve selective charge translocation through their hydrophobic pore.

Two interconnected water wires form an H^+ translocation pathway in AmtB

We next made use of the most substantive body of structural information available for the archetypal ammonium transporter AmtB from *E. coli* and its variants to decipher the molecular mechanism of electrogenic NH_4^+ transport (*Dias Mirandela et al., 2018*). Computational (*Wang et al., 2012*) and experimental studies (*Ariz et al., 2018*) have suggested that deprotonation of NH_4^+ is likely to be a major step in ammonium transport. We therefore aimed to identify dynamic polar networks across AmtB that could form a transfer pathway through the protein for the translocation of H^+, coming from NH_4^+ deprotonation. AmtB forms homotrimers in the cytoplasmic membrane, in which each monomer exhibits a potential periplasmic NH_4^+ binding region (S1) near residue D160, followed by a strongly hydrophobic pore leading towards the cytoplasm (*Figure 2A*; *Khademi et al., 2004*). Two highly conserved histidine residues, H168 and H318, protrude into the lumen, forming the family's characteristic 'twin-His' motif (*Javelle et al., 2006*). The only variation in the twin-His motif in members of the Amt/Mep/Rh family is in numerous fungal Mep transporters where the first His, corresponding to H168, is replaced by a Glu (*Javelle et al., 2006*). The general conservation pattern in the AmtB pore, as analysed with ConSurf (*Ashkenazy et al., 2016*), is shown in *Figure 2—figure supplement 1*.

To locate potential polar transfer routes, we performed atomistic molecular dynamics (MD) simulations of AmtB in mixed lipid bilayers. The simulations initially showed hydration of part of the putative hydrophobic NH_3 pathway from the twin-His motif to the cytoplasm (cytoplasmic water wire –
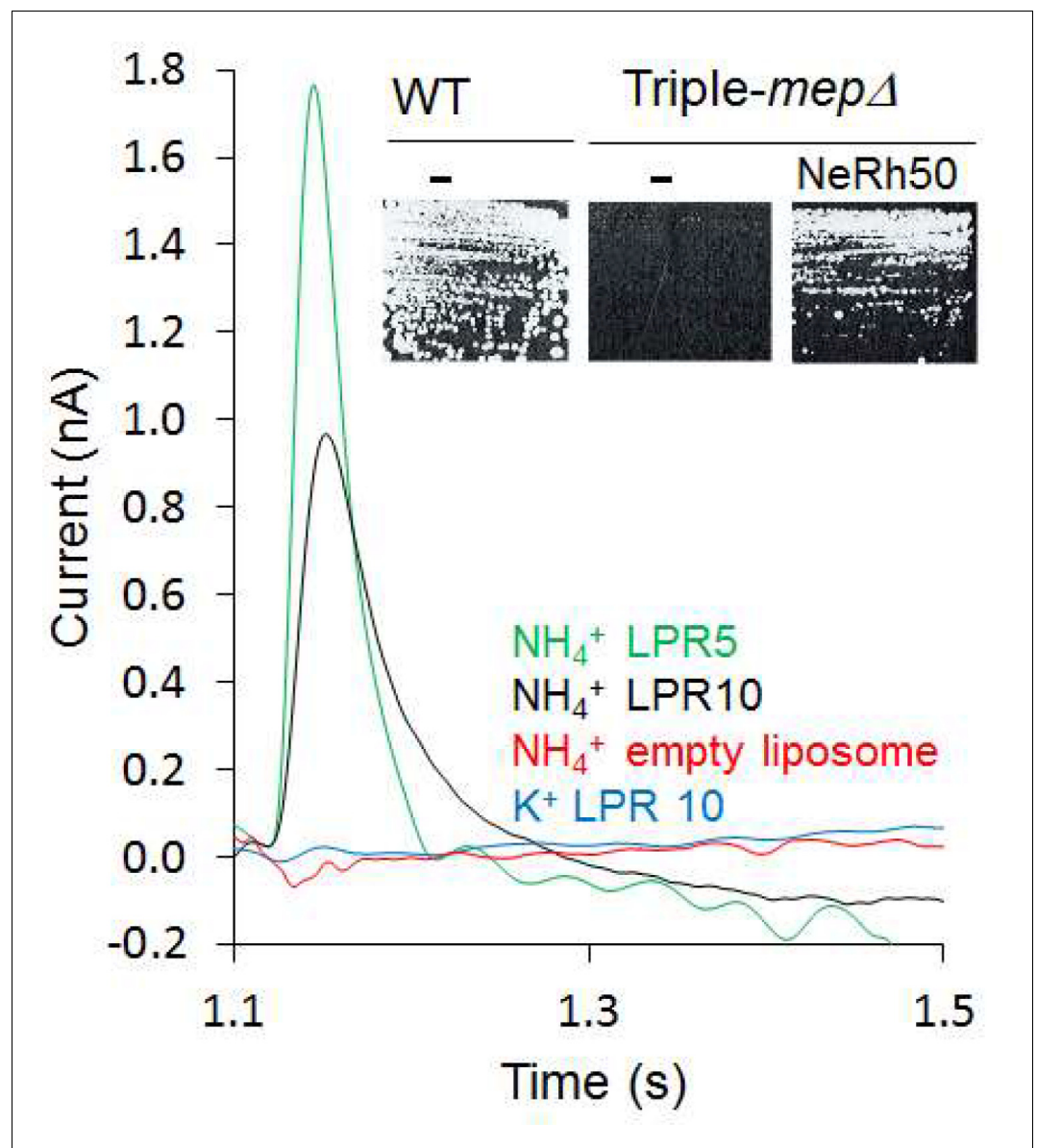
Figure 1. Characterization of the activity of NeRh50. Transient current measured using SSME after a 200 mM pulse (ammonium or potassium). *Insert:* Yeast complementation by NeRh50 (strain 31019b, *mep1Δ mep2Δ mep3Δ ura3*) on minimal medium supplemented with 3 mM ammonium as sole nitrogen source.

The online version of this article includes the following source data and figure supplement(s) for figure 1:

Source data 1. Characterization of the activity of NeRh50.

Figure supplement 1. Characterization of the activity of NeRh50.

CWW; *Figure 2A*), confirming previous observations (*Lamoureux et al., 2007*). Notably, a new observation we made over longer simulation timescales is the presence of a previously unidentified second water-filled channel (periplasmic water wire - PWW). The PWW spans from residue D160 near the S1 region to the central twin-His motif (*Figure 2A*) and is formed both in simulations without and with applied membrane voltage V_m (*Figure 2A* - *Figure 2—figure supplement 2*; V_m in *E. coli* ~ −140 mV [*Felle et al., 1980*]).

As the protonation pattern of the twin-His motif has been found to play a role in the hydration of the protein (*Ishikita and Knapp, 2007*), two different tautomeric states of the twin-His motif were systematically probed in the simulations. The tautomeric state in which H168 is protonated on its N_δ and H318 is protonated on its N_ϵ atom is referred to as 'DE', while 'ED' terms the twin-His

Table 1. Decay time constants (s^{-1}) of transient currents triggered after an ammonium or potassium pulse of 200 mM in proteoliposomes containing AmtB at various LPR*.

	NH_4^+		K^+	
Variant	LPR 10	LPR 5	LPR 10	LPR 5
AmtB-WT	13.4 ± 1.5	18.7 ± 1.0	NC	NC
D160A	21.6 ± 1.2	24.3 ± 1.5	NC	NC
D160E	17.03 ± 2.84	19.53 ± 1.8	NC	NC
H168A H318A	29.5 ± 2.1	29.8 ± 2.6	NC	NC
S219A H168A H318A	NC	NC	NC	NC
H168A	28.3 ± 1.5	38.0 ± 1.0	2.7 ± 0.5	5.2 ± 1.0
H318A	22.56 ± 2.63	28.25 ± 3.1	10.07 ± 1.7	15.64 ± 2.1
NeRh50	24.0 ± 1.7	39.0 ± 3.6	NC	NC

*NC: No transient current recorded.

The online version of this article includes the following source data for Table 1:

Source data 1. Decay time constants (s^{-1}) of transient currents triggered after an ammonium or potassium pulse of 200 mM measured by SSME.
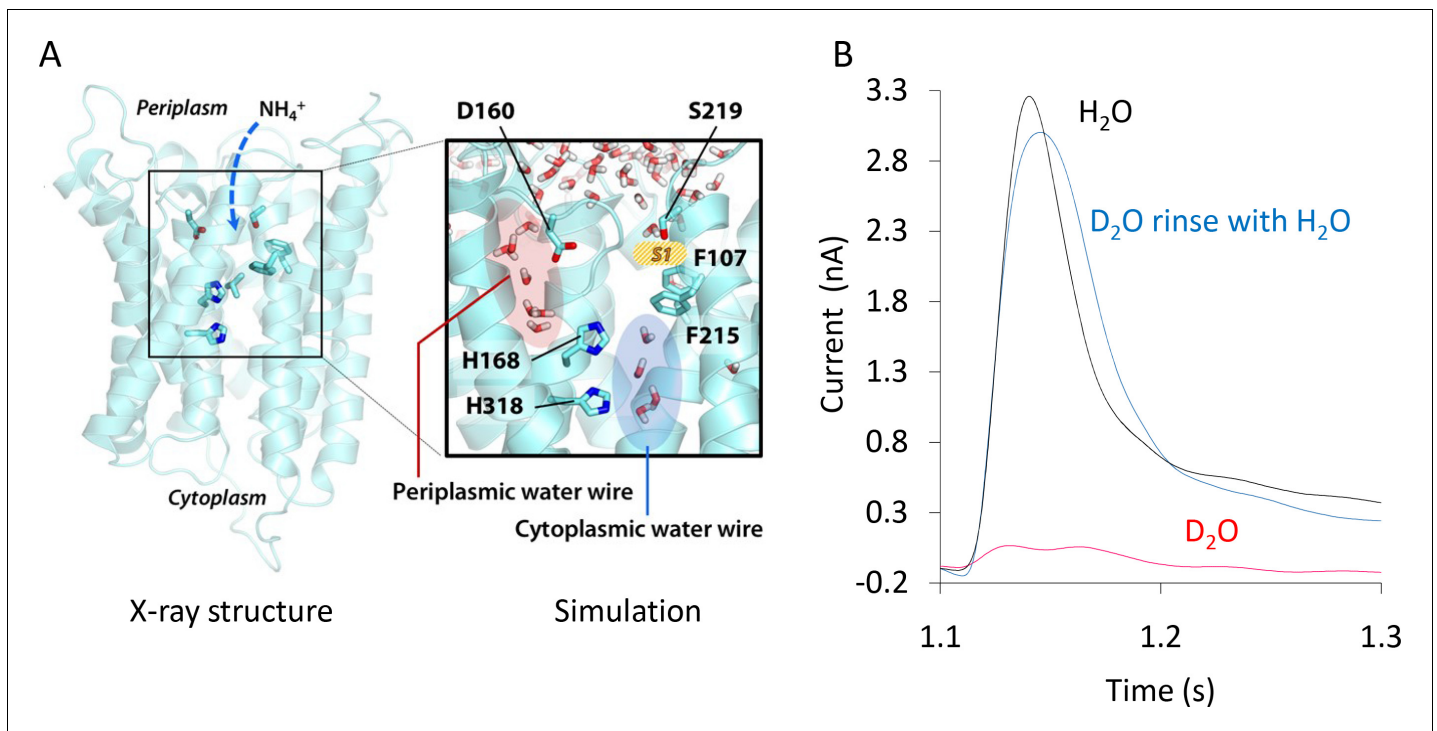
Figure 2. Formation and functionality of the periplasmic (PWW) and cytoplasmic (CWW) water wires in AmtB. (**A**) Extended atomistic simulations show a hydration pattern across the protein, in which cytoplasmic and periplasmic water wires, connected via H168, form a continuous pathway for proton transfer from the S1 NH_4^+ sequestration region to the cytoplasm. (**B**) Transient currents measured following a 200 mM ammonium pulse on sensors prepared with solutions containing either H_2O (black) or D_2O (red). D_2O sensors were rinsed with H_2O solutions and subsequently exposed to another 200 mM ammonium pulse (blue).

The online version of this article includes the following source data and figure supplement(s) for figure 2:

Source data 1. Functionality of the periplasmic (PWW) and cytoplasmic (CWW) water wires in AmtB.

Figure supplement 1. Evolutionary conservation of the proton and hydrophobic pathways for H^+ and NH_3 translocation in AmtB.

Figure supplement 2. Evolution and occupancy of the Periplasmic Water Wire (PWW).

Figure supplement 3. Evolution and occupancy of the Cytoplasmic Water Wire (CWW).

Figure supplement 4. The DE and ED twin-His motif configurations.

configuration where H168 is protonated on N_ε and H318 is protonated on N_δ (*Figure 2A- Figure 2— figure supplement 2*, *3*, *4*). Formation of the CWW is observed to occur within a few nanoseconds at the beginning of each simulation. In the DE tautomeric state, the cytoplasmic pocket of each subunit almost continuously remains occupied by 3–4 water molecules for the rest of the simulation (*Figure 2A - Figure 2—figure supplement 2*, *3*, *4*; data for 0 mV membrane voltage). In the ED state, greater fluctuations in the number of water molecules in the chain are seen, and the average occupancy is decreased. Using a cut-off value of three water molecules per subunit, a complete water chain is present during 79% of the simulations in the DE state, and only during 12% of the simulated time in the ED state. The PWW is generally more transiently occupied than the cytoplasmic channel; however, we record up to 23% occupancy with at least three water molecules when the histidine sidechains are in the ED tautomeric state (*Figure 2A - Figure 2—figure supplement 2*, *3*, *4*).

Both water wires are connected via the twin-His motif, which bridges the aqueous chains, while preventing the formation of a continuous water channel in the simulations. Although neither the CWW nor the PWW are sufficiently wide to allow the transfer of solvated NH_4^+, water molecules and histidine side chains could serve as efficient pathways to facilitate proton transfer in proteins (*Acharya et al., 2010*). As shown in *Figure 2—figure supplement 1*, the key residues that line both water wires in AmtB are highly conserved in the family.

The interconnected water wires are functionally essential to AmtB activity

To experimentally test if the water wires are essential for proton conduction during the AmtB transport cycle, we made use of the reduced deuteron mobility of heavy water D_2O. Because deuterons have twice the mass of a proton and the bond strength is increased, the deuteron mobility is reduced by 30% for each D_2O molecule compared to normal water (*Wiechert and Beitz, 2017*). Since the polar network of water we identified involves more than three water molecules (*Figure 2A*), AmtB should be nearly inactive if tested in the presence of D_2O. Indeed, we found that in an SSME-based assay where all buffers used to prepare the proteoliposomes and SSM sensors were made using D_2O, AmtB activity was completely abolished compared to buffer containing water (*Figure 2B*). After rinsing the sensor prepared in D_2O with water, AmtB re-gained 100% of its activity measured by SSME, showing that the presence of D_2O did not affect the protein itself or the integrity of the proteoliposomes (*Figure 2B*). Further calculations suggested that H^+ transfer between the water molecules is possible both within the PWW and CWW and could occur with high rates (the highest energy barrier is ~18 kJ/mol in the cytoplasmic wire near the twin-His motif; *Table 2*). Taken together, the experimental and computational data suggest that proton transfer between water molecules, most likely the PWW and CWW detected in the simulations, may underpin the electrogenic activity of AmtB.

AmtB activity is not driven by the proton motive force

In the absence of ammonium, a proton pulse did not trigger a discernible current and additionally, in the presence of ammonium, an inward-orientated pH gradient did not increase AmtB activity (*Figure 3*). These findings suggest that there is no H^+-dependent symport activity of AmtB, showing instead that AmtB is not able to translocate a proton in the absence of NH_4^+, and indicating that the current induced by AmtB activity is generated by specific deprotonation of the substrate and subsequent H^+ translocation. Furthermore, they show that AmtB cannot act as an uncoupler, which raises the question of proton selectivity and the coupling between NH_3 and H^+ transfer (*Boogerd et al., 2011*; *Maeda et al., 2019*). Our current data suggest that the PWW is transiently occupied and that its occupancy is strongly dependent on the particular state and conformation of D160, since even a D to E conservative change abolished presence of the PWW (*Figure 4A*). Any disruption of the PWW will, in turn, impede the capability of AmtB to transfer H^+. The functionally relevant conformation and protonation state of D160 that stabilize the PWW is likely to be coupled to the presence of a charged substrate binding near S1, thereby linking substrate binding and deprotonation to H^+ transfer.

Table 2. Free energies for proton translocation through the cytoplasmic and periplasmic water wires and neighboring water molecules (bulk)*.

|				Z (Å)	Free energy (kJ/mol)
(bulk)	Peripl. water wire		wat1	14.7	0.0
			wat2	12.7	8.7
			wat3	10.7	15.0
			wat4	8.3	14.4
			wat5	6.1	7.5
D160			wat6	5.4	11.0
			wat7	3.2	14.4
			wat8	0.6	18.5
H168					
	cytopl. water wire		wat9	−0.4	17.3
			wat10	−0.8	14.4
			wat11	−3.2	12.1
H318			wat12	−5.1	13.8

*The vertical coordinate z was calculated relative to the position of the sidechain of H168. Positions of the sidechains of D160, H168 and H318 with respect to the periplasmic and cytoplasmic water wires are indicated in the left column.

The residue D160 is essential to stabilize the PWW

As the PWW is formed near the sidechain of D160, an invariant residue in the Amt/Mep/Rh super-family (*Marini et al., 2006*; *Thomas et al., 2000*), we further investigated the role of this residue in ensuring PWW and CWW stability by simulating the AmtB D160A and D160E mutants. Both mutants were stable on the time scale of our simulations and we did not detect major rearrangements in the protein. Moreover, all the elution profiles of the purified WT and variants proteins obtained by ana-lytical size exclusion chromatography, before and after solubilization of the proteoliposomes in 2% DDM, were identical, showing a single monodisperse peak eluting between 10.4–10.6 ml (*Figure 4—figure supplement 1*). Taken together, these results suggest that major structural re-arrangements in the mutants are unlikely to occur. The simulations revealed no difference in the formation of the CWW in the D160A and D160E variants compared to the WT, however the formation of the PWW is almost completely abolished in the presence of these mutations (*Figure 4A*).

We then expressed wild-type AmtB as well as the D160A and D160E mutants in *S. cerevisiae* tri-ple-*mepΔ*. Using ammonium as the sole nitrogen source, we found that cells expressing the mutants failed to grow, showing that AmtB[D160A] or AmtB[D160E] are unable to replace the function of the endogenous Mep transporters (*Figure 4B*).

The activity of the purified variants reconstituted into liposomes was next quantified using SSME. Electrogenic transport activity, triggered by a 200 mM ammonium pulse, led to a transient current with a maximum amplitude of 3.38 nA in AmtB, while AmtB[D160A] and AmtB[D160E] displayed reduced maximum currents of 0.63 nA and 1.42 nA respectively (*Figure 4B*, *Figure 4—figure supplement 2*). Importantly, the lifetime of currents in both variants was unaffected by changes in liposomal LPR, and therefore the small transient current accounts for the binding of a NH_4^+ to the proteins and not a full translocation cycle (*Table 1*, *Figure 4—figure supplement 2*; *Bazzone et al., 2017*). Additional-ly, it was impossible to determine with confidence a catalytic constant (K_m) for both variants since no clear saturation was reached, even after an ammonium pulse of 200 mM (*Figure 4C*). These results thus demonstrate that AmtB[D160A] and AmtB[D160E] are transport-deficient. Our data show that residue D160 plays a central role in the transport mechanism as opposed to having a strictly struc-tural role as previously suggested (*Khademi et al., 2004*). Moreover, the fact that the conservative D to E variation at position 160 impairs ammonium transport via AmtB indicates that D160 does not only show electrostatic interaction with NH_4^+ at the S1 site but is also involved in the translocation mechanism by stabilizing the PWW.
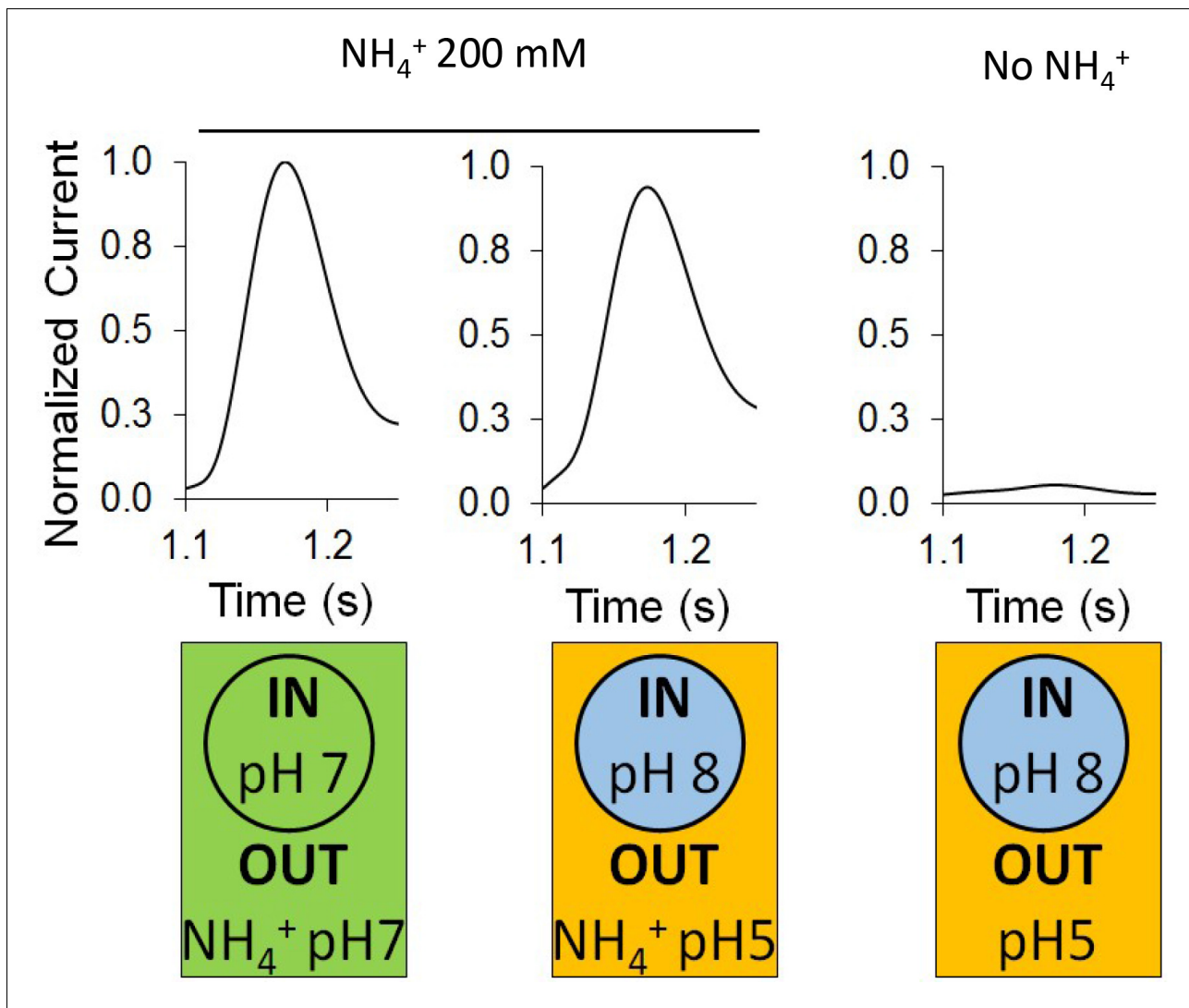
Figure 3. Effect of a proton gradient on AmtB activity. The transient currents were measured using SSME following an ammonium pulse of 200 mM at pH 7 (left) or under an inwardly directed pH gradient in the presence (center) or absence (right) of ammonium. eight sensors from two independent protein purification batches were measured, with three measurements recorded for each sensor. Single representative traces were chosen to visualize the results. Each sensor was measured in the order pH (in/out) 7/7, 8/5, 8/5 (this time without NH_4^+), and finally 7/7 again to be sure that the signals do not significantly decrease with time. The data are normalized against the measurements done at pH7 in/out for each sensor.
The online version of this article includes the following source data for figure 3:

Source data 1. Effect of a proton gradient on AmtB activity.

AmtB switches from transporter to channel-like activity in the absence of the 'twin-His' motif

The CWW and PWW are connected via the twin-His motif, which bridges the aqueous chains, while preventing the formation of a continuous water channel in the simulations (*Figure 2A*). We therefore next probed if the twin-His motif enables proton transfer between the two water wires by recording the activities of twin-His variants. Expressed in *S. cerevisiae* triple-*mepΔ*, AmtB$^{H168A/H318A}$ did not support cell growth on low ammonium (*Figure 5A*). *In-vitro* SSME measurements with this variant displayed LPR-independent current decay rates (*Figure 5A*, *Figure 5—figure supplement 1*, *Table 1*), showing that the residual current is caused by the association of NH_4^+ to AmtB without further transport. No current was recorded for the triple mutant AmtB$^{S219A/H168A/H318A}$, in which binding at the periplasmic face was further altered, confirming that the residual current reflects NH_4^+ interaction near S1 (*Figure 5—figure supplement 1*). The double-His mutant AmtB$^{H168A/H318A}$ is
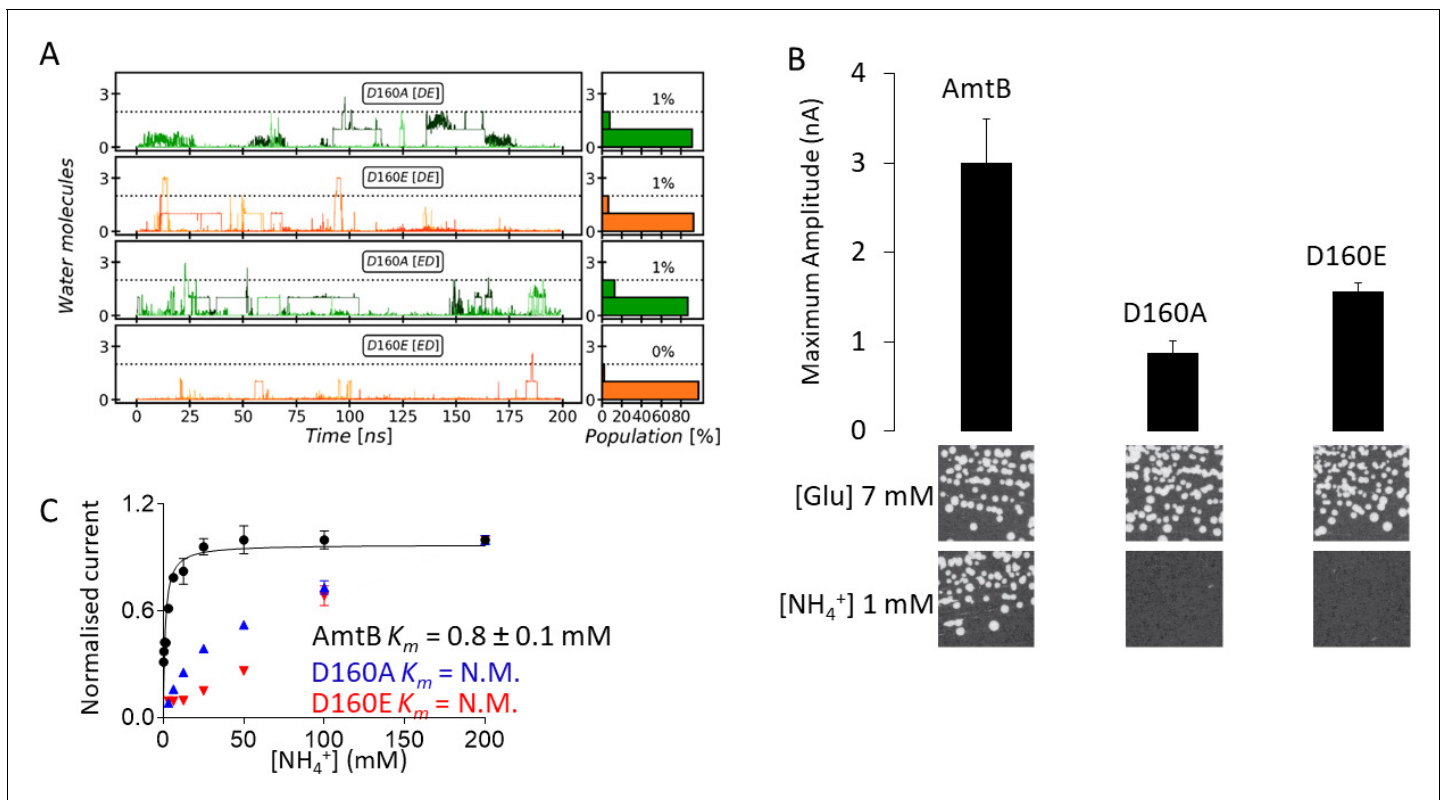
Figure 4. Effect of D160 substitutions. (**A**) The Periplasmic Water Wire (PWW) in the D160A and D160E variants. We observe no significant occupancy of the PWW above the threshold of at least three water molecules in the D160A and D160E AmtB variants, irrespective of the tautomeric protonation states of H168 and H318 (DE or ED, see Materials and method section). (**B**) *Upper panel:* maximum amplitude of the transient current measured using SSME following a 200 mM ammonium pulse. Eight sensors from two independent protein purification batches were measured, with three measurements recorded for each sensor (means ± SD). *Lower panel*: yeast complementation test (strain 31019b, *mep1Δ mep2Δ mep3Δ ura3*) using 7 mM Glutamate (Glu) or 1 mM ammonium as a sole nitrogen source. The growth tests have been repeated twice. (**C**) Kinetics analysis of the transport of ammonium. The maximum amplitudes recorded after a 200 mM ammonium pulse have been normalized to 1.0 for comparison. N.M.: Non Measurable. eight sensors from two independent protein purification batches were measured, with three measurements recorded for each sensor (means ± SD). The online version of this article includes the following source data and figure supplement(s) for figure 4:

Source data 1. Effect of D160 substitutions on AmtB activity measured by SSME.
Figure supplement 1. Size Exclusion Chromatography analysis of AmtB.
Figure supplement 2. Characterization of the activity and specificity of AmtB variants.

thus able to interact with NH_4^+ but cannot transport the substrate across the membrane. This supports our previous structural analysis showing that the CWW in the pore of the double-His mutant AmtB[H168A/H318A] is absent (*Javelle et al., 2006*).

By contrast, the two single histidine-to-alanine substitutions in the twin-His motif unexpectedly produced an LPR-dependent current in our SSME recordings (*Figure 5A*, *Figure 5—figure supplement 1*, *Table 1*). Furthermore, triple-*mepΔ* yeast cells expressing these variants were able to grow in the presence of low ammonium concentrations (*Figure 5A*). Our previous crystal structure (*Javelle et al., 2006*) and our MD simulations (*Figure 5—figure supplement 2*) show increased hydration in the area around A168, which could potentially form a pathway for direct translocation of NH_4^+ without a deprotonation step. To test this hypothesis, we measured the activity of AmtB[H168A] and AmtB[H318A] in D_2O conditions, as described above. Crucially, the activity of both variants measured in the presence or absence of D_2O was similar (*Figure 5B*), in contrast to native AmtB where no activity was recorded in D_2O (*Figure 2B*), showing that proton transfer between water molecules is not a key mechanistic feature in the activity of the mutants. Additionally, the translocation of NH_4^+ is not saturable in the tested concentration range [12.5–200 mM] for AmtB[H168A] and AmtB[H318A] (*Figure 5C*). Summarizing, these results suggest that AmtB switches from
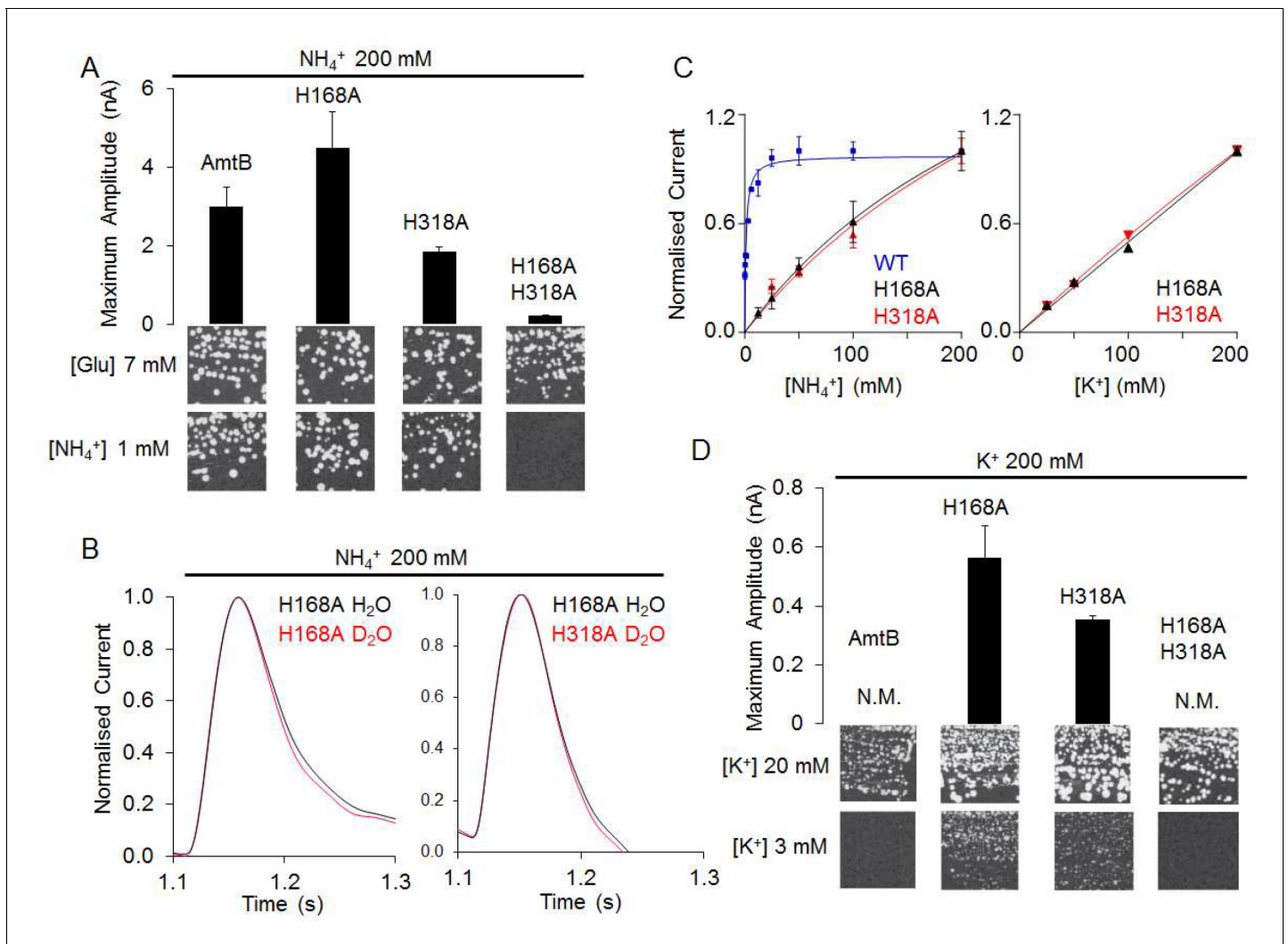
Figure 5. The AmtB[H168A] and AmtB[H318A] lose their specificity toward ammonium. (**A**) *Upper panels:* maximum amplitude of the transient current measure using SSME after a 200 mM ammonium pulse. Eight sensors from two independent protein purification batches were measured, with three measurements recorded for each sensor (means ± SD). *Lower panels:* yeast complementation test (strain 31019b, *mep1Δ mep2Δ mep3Δ ura3*) using 7 mM Glutamate (Glu) or 1 mM ammonium as a sole nitrogen source. The growth tests have been repeated twice. (**B**) Transient currents measured using SSME following a 200 mM ammonium pulse on sensors prepared with solutions containing either H_2O (black) or D_2O (red). The maximum amplitudes recorded after a 200 mM ammonium pulse on sensor prepared in H_2O have been normalized to 1.0 for comparison. eight sensors from two independent protein purification batches were measured, with three measurements recorded for each sensor (means ± SD). (**C**) Kinetics analysis of the transport of NH_4^+ (or K^+ in AmtB[H168A] (black), AmtB[H318A] (red) and WT-AmtB (bleu, only for NH_4^+, as no signal was measurable with K^+). The maximum amplitudes recorded after a 200 mM NH_4^+ or K^+ pulse have been normalized to 1.0 for comparison. Eight sensors from two independent protein purification batches were measured, with three measurements recorded for each sensor (means ± SD). (**D**) *Upper panels:* maximum amplitude of the transient current measured using SSME after a 200 mM potassium pulse. N.M. Non Measurable. Eight sensors from two independent protein purification batches were measured, with three measurements recorded for each sensor (means ± SD). *Lower panels:* yeast complementation test (strain #228, *mep1Δ mep2Δ mep3Δ trk1Δ trk2Δ leu2 ura3*) using media supplemented with 20 mM or 3 mM KCl. The growth test has been repeated twice.

The online version of this article includes the following source data and figure supplement(s) for figure 5:

Source data 1. Effect of H168 and/or H318 substitution on AmtB activity and selectivity measured by SSME.

Figure supplement 1. Characterization of the activity and specificity of AmtB variants.

Figure supplement 2. MD simulation of AmtB[H168A] showing formation of a continuous water wire traversing the central pore region.
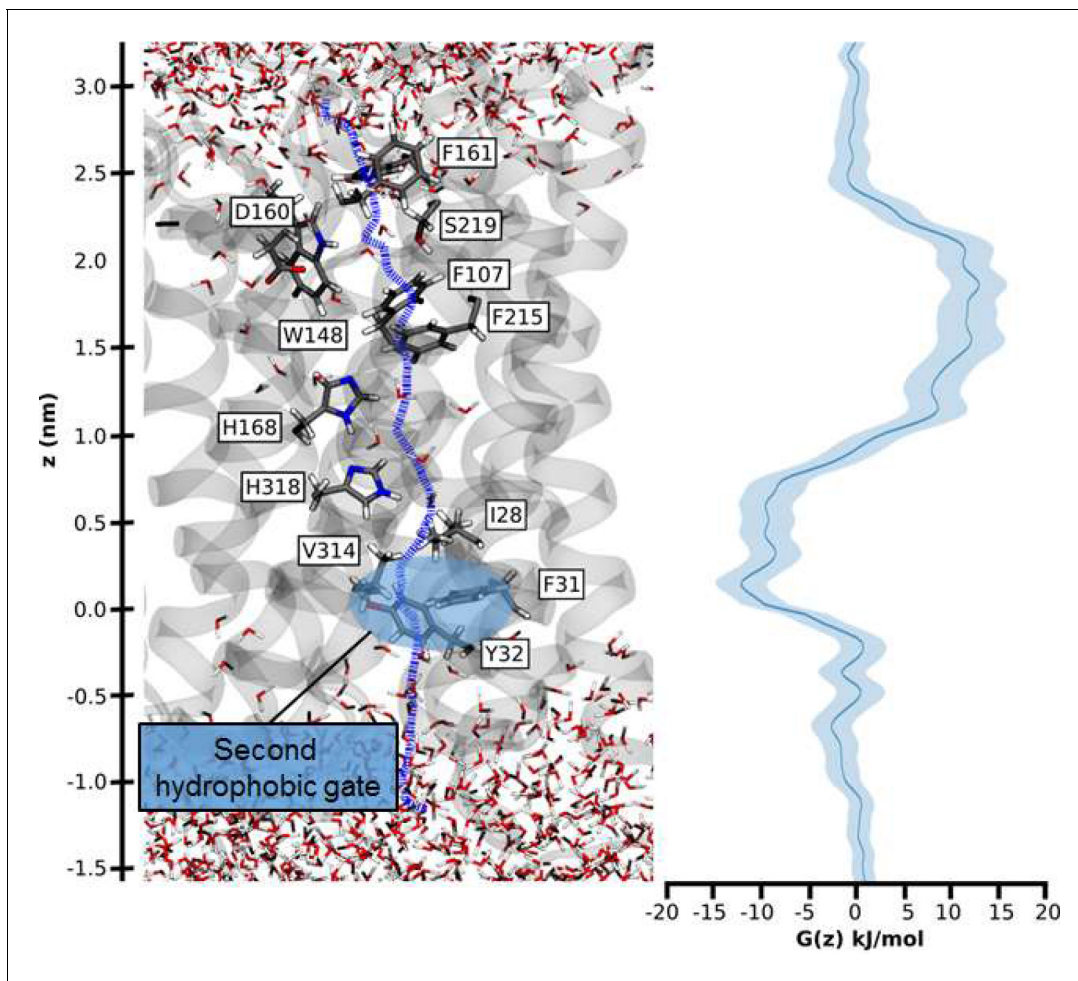
Figure 6. Hydrophobic pathway and energetics for NH_3 translocation in AmtB. We probed an optimal pathway for NH_3 transfer during our PMF calculations (left, purple dash trajectory) in the presence of both the PWW and CWW. The software HOLE (49) was used to determine the most likely transfer route. The pathway from the periplasm to the cytoplasm traverses the hydrophobic gate region (F107 and F215), crosses the cavity next to the twin-His motif (H168 and H318) occupied by the CWW, and continues across a second hydrophobic region (I28, V314, F31, Y32) before entering the cytoplasm.

transporter- to channel-like activity in the absence of the twin-His motif, directly translocating hydrated NH_4^+ through the pore. In the wild-types of Amt/Mep/Rh protein family members, the twin-His motif is highly conserved, which shows that transporter, as opposed to channel activity, is mechanistically crucial for the function of these proteins. The only variation seen in naturally occurring sequences is a replacement of the first His by Glu in some fungal Mep proteins (*Javelle et al., 2006*; *Thomas et al., 2000*). Channel activity is so far only observed for the alanine mutants, not the wild-type. We hypothesized that transport activity might thus be key to ensure ion selectivity of AmtB, since NH_4^+ and K^+ are cations of similar size and hydration energy (*Aydin et al., 2020*).

The twin-His motif interconnects the two water wires to ensure the selectivity of AmtB

Since NH_4^+ was directly translocated in the absence of the twin-his motif and earlier studies implicated a role of the motif in AmtB selectivity (*Ganz et al., 2020*; *Hall and Yan, 2013*), we repeated our SSME experiments on the AmtB[H168A] and AmtB[H318A] variants using the competing K^+ ion as substrate. A 200 mM K^+ pulse triggered currents in both variants, whose decay rates strongly depended on the LPR (*Figure 5D*, *Table 1*, *Figure 5—figure supplement 1*). Furthermore, the single His variants, but not native AmtB, complemented the growth defect of a yeast strain lacking its three endogenous ammonium (Mep) and potassium (Trk) transporters when a limited concentration
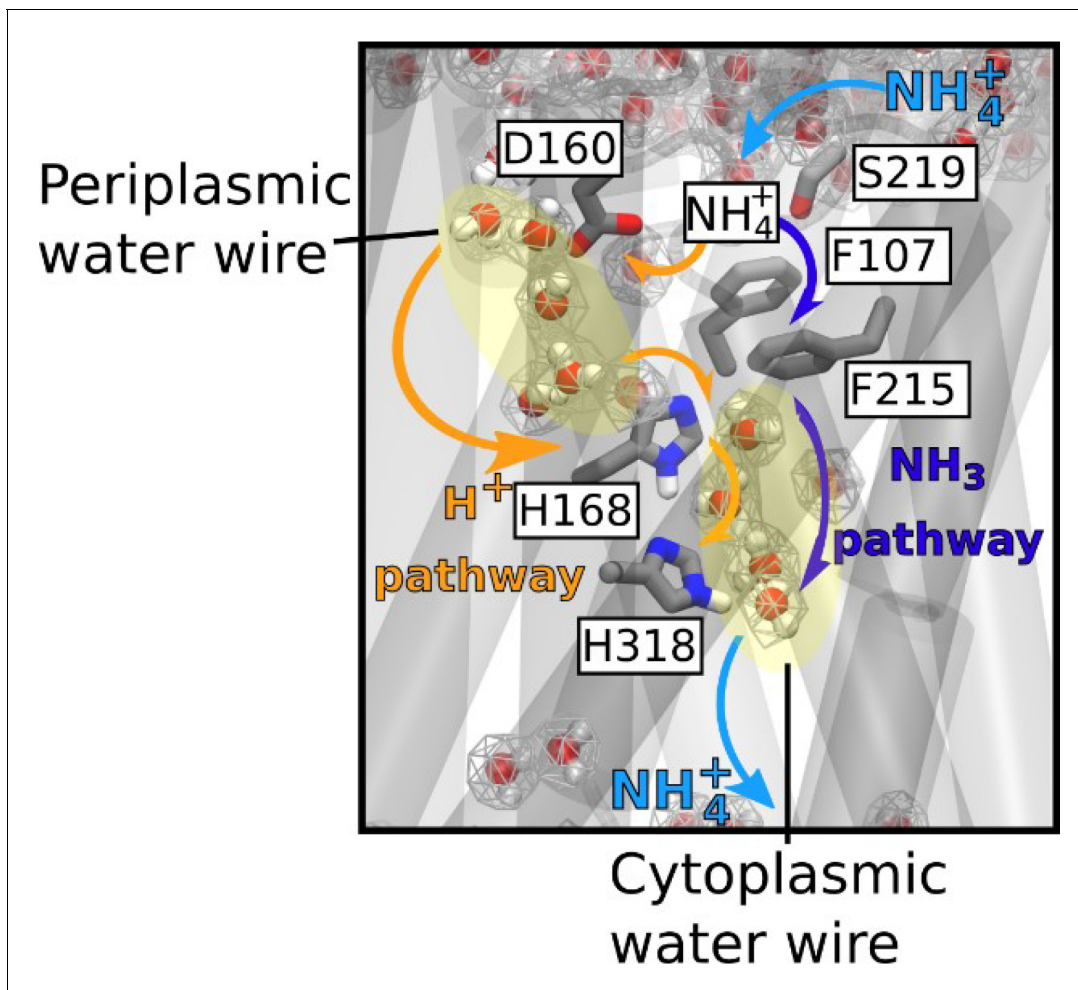
Figure 7. Mechanism of electrogenic NH_4^+ translocation in AmtB. Following sequestration of NH_4^+ at the periplasmic face, NH_4^+ is deprotonated and H^+ and NH_3 follow two separated pathways to the cytoplasm (orange arrows depict the pathway for H^+ transfer, dark blue arrows for NH_3), facilitated by the presence of two internal water wires. NH_3 reprotonation likely occurs near the cytoplasmic exit (*Figure 6*). The hydrated regions within the protein as observed in simulations are highlighted by wireframe representation, crucial residues involved in the transport mechanism are shown as sticks.

of K^+ was present (*Figure 5D*). The K^+ translocation activity is not saturable in the substrate range [12.5–200 mM] (*Figure 5C*). These results demonstrate that both variants, AmtB[H168A] and AmtB[H318A], translocate K^+ ions across the membrane. The substitutions within the twin-His motif thus abolished selectivity for NH_4^+.

The presence of both histidine residues is therefore critical in ammonium transport, since permeability of ammonium transporters for K^+ would compromise ionic homeostasis and disrupt the membrane potential of *E. coli* cells, which crucially depends on maintaining K^+ concentration gradients across the membrane. Moreover, since AmtB is expressed in *E. coli* under nitrogen starvation conditions (low NH_4^+/K^+ ratio), loss of selectivity for NH_4^+ would impede ammonium uptake. Our results thus demonstrate that the twin-His motif, which is highly conserved amongst members of the family, is an essential functional element in the transport mechanism, preventing the transport of competing cations, whilst providing a pathway for proton transfer by bridging the periplasmic and the cytoplasmic water wires.

NH_3 permeation through the hydrophobic pore

Umbrella sampling free-energy calculations were performed to establish the rate limiting step of NH_4^+ transport. Our calculations show that NH_3 translocation experiences only a moderate energy barrier (~10 kJ/mol) at the periplasmic hydrophobic constriction region (F107 and F215) (*Figure 6*).

The starting points of the sampling windows were determined from the centers of HOLE calculations (**Smart et al., 1996**), optimizing the pathway of NH_3 translocation across the pore. A possible influence from this selection regarding the pathway was further reduced by allowing the molecule to move freely perpendicular to the pore axis within a radius of 5 Å in addition to extensive sampling; however, residual bias from window selection cannot be completely excluded. From the free energy profile of NH_3 translocation, we identified a shallow binding site below the twin-His motif (~5 kJ/mol). This is followed by a second hydrophobic region (I28, V314, F31 and Y32) that forms a small energy barrier between this binding site and the cytoplasmic exit. The increased residence time of NH_3 within this energy minimum suggests that reprotonation to NH_4^+, caused by the cytoplasmic pH, occurs in this region (**Figure 6**). Since both energy barriers for H^+ transfer along the water chains and NH_3 permeation are relatively small, we concluded that either initial deprotonation or proton transfer across the twin-His motif could be rate-limiting for overall NH_4^+ transport.

Conclusion

A new model for the mechanism of electrogenic ammonium transport therefore emerges from our findings (**Figure 7**). After deprotonation of NH_4^+ at the periplasmic side, a previously undiscovered polar conduction route enables H^+ transfer into the cytoplasm. A parallel pathway, lined by hydrophobic groups within the protein core, facilitates the simultaneous transfer of uncharged NH_3, driven by concentration differences. On the cytoplasmic face, the pH of the cell interior leads to recombination to NH_4^+, most likely near a second hydrophobic gate (**Figure 6**). The twin-His motif, which bridges the water chains constitutes the major selectivity gate for NH_4^+ transport preventing K^+ flow. We propose that this mechanism is conserved amongst the electrogenic members of the Amt/Mep/Rh family. Importantly, two RhAG polymorphisms associated to the overhydrated stomatocytosis human syndrome have also acquired the ability to transport K^+. Thus, deciphering the transport mechanism of two archetypal members of the family such as AmtB and NeRh50 could bring new insights to the understanding of substrate specificity determinants in Rh proteins in the context of human diseases (**Bruce et al., 2009**).

Our findings define a new mechanism, by which ionizable molecules that are usually charged in solution are selectively and efficiently transported across a highly hydrophobic environment like the AmtB/Rh pore. Alongside size-exclusion and ion desolvation (**Kopec et al., 2018**), it adds a new principle by which selectivity against competing ions can be achieved. Other biological transport systems, like the formate/nitrite transporters, may share similar mechanisms involving deprotonation-reprotonation cycles (**Wiechert and Beitz, 2017**).

Materials and methods

Key resources table

Reagent type (species) or resource	Designation	Source or reference	Identifiers	Additional information
Gene (*Escherichia coli*)	AmtB	**Zheng et al., 2004**	Uniprot: C3TLL2	
Gene (*Nitrosomonas europea*)	Rh50	**Lupo et al., 2007**	Uniprot Q82 × 47	
Strain, strain background (*Escherichia coli*)	C43 (DE3)	**Miroux and Walker, 1996**		Chemically competent cells
Strain, strain background (*Escherichia coli*)	GT1000	**Javelle et al., 2004**		Chemically competent cells
Recombinant DNA reagent	pET22b (+)	Novagen	Cat# - 69744	
Recombinant DNA reagent	pDR195	**Rentsch et al., 1995**	Addgene - 36028	High copy yeast expression vector
Recombinant DNA reagent	pAD7	**Cherif-Zahar et al., 2007**		pESV2-RH50(His)₆

Continued on next page

Continued

Reagent type (species) or resource	Designation	Source or reference	Identifiers	Additional information
Recombinant DNA reagent	p426MET25	*Mumberg et al., 1994*		
Recombinant DNA reagent	PZheng	*Zheng et al., 2004*		pET22b-AmtB(His)$_6$
Recombinant DNA reagent	pGDM2	This study		pET22b-AmtB(His)$_6^{H168AH318A}$
Recombinant DNA reagent	pGDM4	This study		pET22b-AmtB(His)$_6^{D160A}$
Recombinant DNA reagent	pGDM5	This study		pET22b-AmtB(His)$_6^{D160E}$
Recombinant DNA reagent	pGDM6	This study		pET22b-AmtB(His)$_6^{S219AH168AH318A}$
Recombinant DNA reagent	pGW2	This study		pET22b-AmtB(His)$_6^{H168A}$
Recombinant DNA reagent	pGDM9	This study		pDR195-AmtB(His)$_6^{D160A}$
Recombinant DNA reagent	pGDM10	This study		pDR195-AmtB(His)$_6^{D160E}$
Recombinant DNA reagent	pGDM12	This study		pDR195-AmtB(His)$_6^{H168AH318A}$
Recombinant DNA reagent	pGDM13	This study		pDR195-AmtB(His)$_6^{S219AH168AH318A}$
Recombinant DNA reagent	pGW7	This study		pDR195-AmtB(His)$_6^{H168A}$
Sequence-based reagent	AmtB^{S219A} F	IDT	PCR Primer (Mutagenesis)	GGTGGCACCGTGGTGG**ATA**TTAACGCCGCAATC
Sequence-based reagent	AmtB^{D160A} F	IDT	PCR Primer (Mutagenesis)	CTCACGGTGCGCTGG**CC**TTCGCGGGTGGCACC
Sequence-based reagent	AmtB^{D160E} F	IDT	PCR Primer (Mutagenesis)	CTCACGGTGCGCTGG**AG**TTCGCGGGTGGCACC
Sequence-based reagent	AmtB^{H168A} F	IDT	PCR Primer (Mutagenesis)	GGTGGCACCGTGGTGG**CCA**TTAACGCCGCAATC
Sequence-based reagent	AmtB^{H318A} F	IDT	PCR Primer (Mutagenesis)	TGTCTTCGGTGT**GGC**CGGCGTTTGTGGCATT
Sequence-based reagent	AmtB XhoI	IDT	PCR primer	AGTC**CTCGAG**ATGAAGATAGCGACGATAAAA
Sequence-based reagent	AmtB BamHI	IDT	PCR primer	AGTC**GGATCC**TCACGCGTTATAGGCATTCTC
Sequence-based reagent	P5'NeRh	IDT	PCR primer	GCC**ACTAGT**ATGAGTAAACACCTATGTTTC
Sequence-based reagent	P3'NeRh	IDT	PCR primer	GCC**GAATTC**CTATCCTTCTGACTTGGCAC
Peptide, recombinant protein	AmtB(His)$_6$	This study		purified from *E. coli* C43 (DE3) cells
Peptide, recombinant protein	AmtB(His)$_6^{D160A}$	This study		purified from *E. coli* C43 (DE3) cells
Peptide, recombinant protein	AmtB(His)$_6^{D160E}$	This study		purified from *E. coli* C43 (DE3) cells
Peptide, recombinant protein	AmtB(His)$_6^{H168AH318A}$	This study		purified from *E. coli* C43 (DE3) cells

Continued on next page

Continued

Reagent type (species) or resource	Designation	Source or reference	Identifiers	Additional information
Peptide, recombinant protein	AmtB (His)$_6$^{S219AH168AH318A}	This study		purified from *E. coli* C43 (DE3) cells
Peptide, recombinant protein	AmtB(His)$_6$^{H168A}	This study		purified from *E. coli* C43 (DE3) cells
Peptide, recombinant protein	AmtB(His)$_6$^{H318A}	This study		purified from *E. coli* C43 (DE3) cells
Peptide, recombinant protein	*Ne*Rh50(His)$_6$	This study		purified from *E. coli* C43 GT1000 cells
Peptide, recombinant protein	XhoI	Promega	Cat# - R6161	
Peptide, recombinant protein	BamHI	Promega	Cat# - R6021	
Commercial assay or kit	Quikchange XL site-directed mutagensis kit	Agilent Technologies	Cat# 200516	
Chemical compound, drug	n-dodecyl-β-D-maltopyranoside (DDM)	Avanti	Cat#- 850520	
Chemical compound, drug	lauryldecylamine oxide (LDAO)	Avanti	Cat#- 850545	
Chemical compound, drug	*E. coli* Polar Lipids	Avanti	Cat#−100600	
Chemical compound, drug	Phosphotidylcholine (POPC)	Avanti	Cat#−850457	
Software, algorithm	Graphpad Prism software	GraphPad Prism (https://www.graphpad.com)		Version 6.01
Software, algorithm	Origin Pro Software	Origin Labs (https://www.originlab.com)		Origin 2017 Version 94E
Software, algorithm	SURFE^{2}R Control Software	Nanion (https://www.nanion.de/en/)		V1.5.3.2

Mutagenesis

AmtB mutants were generated using the Quikchange XL site-directed mutagenesis kit (Agilent Technologies), according to the manufacturer's instructions. The primers used for mutagenesis are listed in Key resources table. The template was the *amtB* gene cloned into the plasmid pET22b(+), as previously described (*Zheng et al., 2004*; Key resources table).

AmtB and NeRh50 expression in yeast and complementation test

The different variants of *amtB* were amplified using *amtB* cloned into pET22b(+) (Key resources table) as a template with the primers AmtB XhoI and AmtB BamHI (Key resources table) and then sub-cloned into the plasmids pDR195 (Key resources table). The NeRh50 gene was amplified from *N. europaea* genomic DNA (kind gift from Daniel J. Arp and Norman G. Hommes, Department of Botany and Plant Pathology, Oregon State University, Corvallis, USA) using the primers P5'NeRh and P3'NeRh (Key resources table), and was then cloned into the SpeI and EcoRI restriction sites of the high-copy vector p426Met25 (Key resources table), allowing controlled-expression of NeRh50 by the yeast methionine repressible MET25 promoter.

Saccharomyces cerevisiae strains used in this study are the 31019b strain (*mep1Δ mep2Δ mep3Δ ura3*) and the #228 strain (*mep1Δ mep2Δ mep3Δ trk1Δ trk2Δ leu2 ura3*) (*Hoopen et al., 2010*; *Marini et al., 1997*). The plasmids used in this study are listed in Key resources table. Cell transformation was performed as described previously (*Gietz et al., 1992*). For growth tests on limiting ammonium concentrations, yeast cells were grown in minimal buffered (pH 6.1) medium and for growth tests on limiting potassium concentrations, a minimal buffered (pH 6.1) medium deprived of potassium salts was used (*Jacobs et al., 1980*). 3% glucose was used as the carbon source and, 0.1% glutamate, 0.1% glutamine or $(NH_4)_2SO_4$ at the specified concentrations were used as the nitrogen sources.

All growth experiments were repeated at least twice.

Protein purification

AmtB(His$_6$) cloned into the pET22b(+) vector (Key resources table) was overexpressed and purified as described previously (*Zheng et al., 2004*). The plasmid pAD7 (Key resources table) was used to overexpress NeRh50 in the *E. coli* strain GT1000 (*Javelle et al., 2004*). GT1000 was transformed with pAD7 and grown in M9 medium (*Elbing and Brent, 2002*), in which ammonium was replaced by 200 μg/ml glutamine as sole nitrogen source. NeRh50 was purified as described by *Lupo et al., 2007* with minor modifications, namely: the membrane was solubilized using 2% lauryldecylamine oxide (LDAO) instead of 5% *n*-octyl-β-D-glucopyranoside (OG), and 0.09% LDAO was used in place of 0.5% β-OG in the final size exclusion chromatography buffer (50 mL Tris pH 7.8, 100 mL NaCl, 0.09% LDAO).

AmtB and NeRh50 insertion into proteoliposomes

AmtB and NeRh50 were inserted into liposomes containing *E. coli* polar lipids/phosphatidylcholine (POPC) 2/1(wt/wt) as previously described (*Mirandela et al., 2019*). For each AmtB variant, proteoliposomes were prepared at lipid-to-protein ratios (LPRs) of 5, 10, and 50 (wt/wt). The size distribution of proteoliposomes was measured by dynamic light scattering (DLS) using a Zetasizer Nano ZS (Malvern Instruments, Malvern, UK). This analysis showed that the proteoliposomes had an average diameter of 110 nm (*Figure 8*). Proteoliposomes were divided into 100 μL aliquots and stored at −80°C.

To ensure that all AmtB variants were correctly inserted into the proteoliposomes, the proteoliposomes were solubilized in 2% DDM and the proteins analyzed by size exclusion chromatography using a superdex 200 (10 × 300) enhanced column. The elution profile of all variants and the wildtype were identical, showing a single monodisperse peak eluting between 10.4–10.6 ml (*Figure 4—figure supplement 1*). This demonstrated that all proteins were correctly folded, as trimers, in the proteoliposomes.

Solid supported membrane electrophysiology

To form the solid-supported membrane, 3 mm gold-plated sensors were prepared according to the manufacturer's instructions (Nanion Technologies, Munich, Germany), as described previously (*Bazzone et al., 2017*). Proteoliposomes/empty liposomes were defrosted and sonicated in a sonication bath at 35 W for 1 min, diluted 10 times in non-activating (NA) solution (*Supplementary file 1*), and then 10 μl were added at the surface of the SSM on the sensor. After centrifugation, the sensors were stored at 4°C for a maximum of 48 hr before electrophysiological measurements. For the D_2O experiments, all the solutions were prepared using D_2O instead of water.

All measurements were made at room temperature (21°C) using a SURFE^{2}R N1 apparatus (Nanion Technologies, Munich, Germany) with default parameters (*Bazzone et al., 2017*). Prior to any measurements, the quality of the sensors was determined by measuring their capacitance (15–30 nF) and conductance (<5 nS).

For functional measurements at a fixed pH, a single solution exchange protocol was used with each phase lasting 1 s (*Bazzone et al., 2017*). First, non-active (NA) solution was injected onto the sensor, followed by activating (A) solution containing the substrate at the desired concentration and finally NA solution (*Supplementary file 1*).

For the measurements under inwardly orientated pH gradient, a double solution exchange protocol was used (*Bazzone et al., 2017*), in which an additional resting solution phase of 15 min in NA solution at pH 8 was added to the end. The incubation phase adjusts the inner pH of the proteoliposomes to
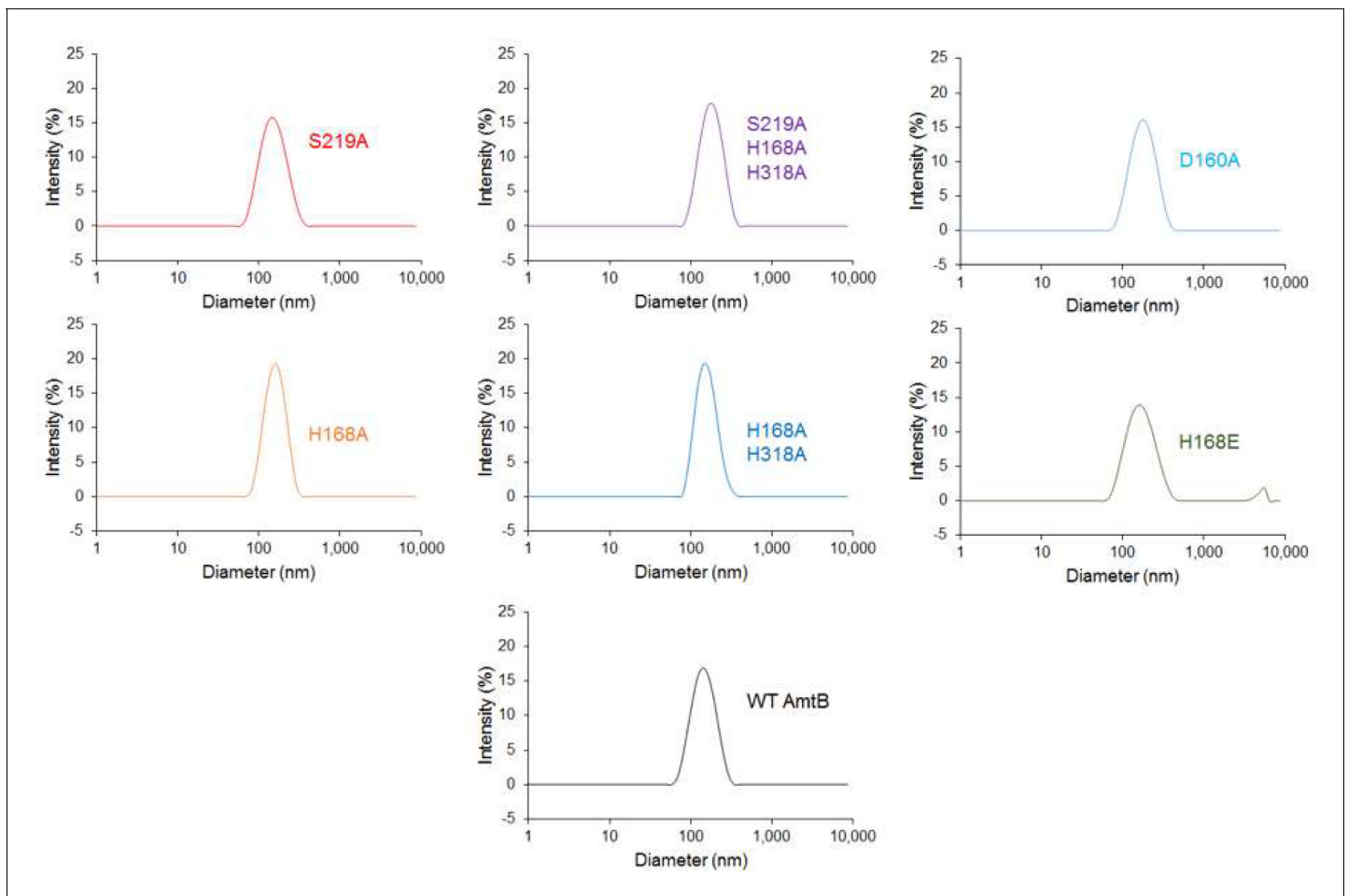
Figure 8. Size distribution of the proteoliposomes containing wild-type and variants of AmtB. Dynamic light scattering was used to determine the number-weighted distribution of liposome sizes in the detection reagent. The distribution was monodisperse, with a mean diameter of 110 nm.

pH 8 and establishes a pH gradient at the beginning of each measurement by pulsing the activation solution at pH 5.

Each sensor was measured in the order pH (in/out) 7/7, 8/5 (with NH_4^+), 8/5 (without NH_4^+), and finally again 7/7 to ensure that the signals do not significantly decrease with time. The data are normalized against the measurements conducted at pH7 in/out for each sensor. All measurements were recorded on 8 sensors from two independent protein purification batches, with 3 measurements recorded for each sensor.

The kinetic parameters were calculated using Graphpad Prism 6 (GraphPad Software, San Diego, California, USA) and fitted according to the Michaelis-Menten equation (Key resources table). Lifetime analysis of the current (decay time of the transient current) was performed to differentiate small pre-steady state currents, which arise due to the binding of a charged species to membrane proteins, from currents reflecting full transport cycles, which show faster decay rates under raised liposomal LPR (*Bazzone et al., 2017*). The decay time of the transient current (*Table 1*) was calculated by fitting the raw transient current data between the apex of the peak and the baseline (after transport) with a non-linear regression using OriginPro 2017 (OriginLab, Northampton, Massachusetts, USA). The regression was done using a one-phase exponential decay function with time constant parameter:

$$y = y_0 = A_1 e^{-x/t_1}$$

The fit was obtained using the Levenberg-Marquardt iteration algorithm, where x and y represent coordinates on the respective axis, y_0 represents the offset at a given point, A represents the amplitude, and t is the time constant.

Molecular Dynamics simulations

The AmtB trimer (PDB code: 1U7G) (*Khademi et al., 2004*) was processed using the CHARMM-GUI web server (*Lee et al., 2016*). Any mutations inserted during the crystallization process were reverted to the wild-type form. The N-termini and C-termini of the subunits were capped with acetyl and N-methyl amide moieties, respectively. The protein was then inserted into a membrane patch of *xy*-dimensions 13 × 13 nm. Unless otherwise specified, a membrane composition of palmitoyl oleoyl phosphatidyl ethanolamine and palmitoyl oleoyl phosphatidyl glycine (POPE/POPG) at a 3:1 ratio was used in order to approximate the composition of a bacterial cytoplasmic membrane. We employed the CHARMM36 forcefield for the protein and counter ions (*Best et al., 2012*). The water molecules were modeled with the TIP3P model (*Jorgensen et al., 1983*). Water bonds and distances were constrained by the Settle method (*Miyamoto and Kollman, 1992*), and all other bonds by the LINCS method (*Hess et al., 1997*). In simulations without ammonium, K^+ and Cl^- ions were added to neutralize the system and obtain a bulk ionic concentration of 250 mM. In simulations with ammonium, K^+ was replaced by NH_4^+. The parameters for NH_4^+ and NH_3 (umbrella sampling simulations) were adapted from *Nygaard et al., 2006*.

After a steepest descent energy minimization, the system was equilibrated by six consecutive equilibration steps using position restraints on heavy atoms of 1000 kJ/mol.nm^2. The first three equilibration steps were conducted in an NVT ensemble, applying a Berendsen thermostat (*Berendsen et al., 1984*) to keep the temperature at 310K. The subsequent steps were conducted under an NPT ensemble, using a Berendsen barostat (*Berendsen et al., 1984*) to keep the pressure at 1 bar. Production molecular dynamics simulations were carried out using a v-rescale thermostat (*Bussi et al., 2007*) with a time constant of 0.2 ps, and a Berendsen barostat with semi-isotropic coupling. A timestep of 2 fs was used throughout the simulations.

In a subset of simulations, we aimed to test the effect of membrane voltage on the internal hydration of AmtB using CompEL. For the CompEL simulations (*Kutzner et al., 2016*), the system was duplicated along the z-axis, perpendicular to the membrane surface. To focus on the physiologically relevant voltage gradient in *E. coli*, that is a negative potential on the inside of the cell of magnitude −140 to −170 mV (*Cohen and Venkatachalam, 2014*), an antiparallel orientation of the two trimers in the double bilayers was used (*Felle et al., 1980*). The final double system consisted of a rectangular box of 13 × 13×20 nm. For the CompEL simulations, 1000 positively charged (either NH_4^+ or K^+) and 1000 negatively charged ions (Cl^-) were added to the system, then the system was neutralized, and the desired ion imbalance established.

The Umbrella Sampling (US) Potential-of-Mean-Force (PMF) calculations (*Torrie and Valleau, 1977*) were set up as described previously by *Hub et al., 2010b*. A snapshot was taken from the simulation of the single bilayer system with the twin-His motif in the DE protonation state and both the CWW and PWW occupied. The pore coordinates were obtained using the software HOLE (*Smart et al., 1996*), removing the solvent and mutating F215 to alanine during the HOLE run only. Starting coordinates for each umbrella window were generated by placing NH_3 in the central x-y coordinate of the pore defined by HOLE at positions every 0.5 Å in the z coordinate. Solvent molecules within 2 Å of the ammonia's N atom were removed. Minimization and equilibration were then re-performed as described above. Unless otherwise stated, position restraints were used for all water oxygen atoms in the CWW with a 200 kJ/mol.nm^2 force constant; while the TIP3 molecules within the lower water wire were not restrained. For the US the N atom of ammonia was position-restrained with a force constant of 1000 kJ/mol.nm^2 on the z axis and a 400 kJ/mol.nm^2 cylindrical flat-bottomed potential with a radius of 5 Å in the x-y plane, as described earlier by *Hub et al., 2010a*. For some US window simulations, the ammonia z-axis restraints were increased and the time step reduced in the equilibration to relax steric clashes between sidechains and ammonia. After equilibration, US simulations were run for 10ns, using the parameters described above (*Lee et al., 2016*) and removing the initial two ns for further equilibration. The PMF profiles were generated with the GROMACS implementation of the weighted histogram analysis method (WHAM) with the periodic implementation (*Hub et al., 2010a*). Further US simulations were performed to as needed to improve sampling in regions of the profile that were not sufficiently sampled. The Bayesian bootstrap method was performed with 200 runs to calculate the standard deviation of the PMF.

Free energy calculations for proton translocation

The free energies for proton translocation were evaluated by protonating the water molecules at different sites along the periplasmic and cytoplasmic water wires. Electrostatic effects in proteins are often treated more effectively using semi-macroscopic models which can overcome the convergence problems of more rigorous microscopic models. Here we used the semi-macroscopic protein dipole/ Langevin dipole approach of Warshel and coworkers in the linear response approximation version (PDLD/S-LRA) (*Kato et al., 2006*; *Sham et al., 2000*). Positions of the water molecules in the PWW and CWW were obtained from the corresponding MD snapshots (*Figure 1*). All PDLD/S-LRA pK_a calculations were performed using the automated procedure in the MOLARIS simulations package (*Lee et al., 1993*) in combination with the ENZYMIX force field. The simulation included the use of the surface-constrained all atom solvent model (SCAAS) (*Warshel and King, 1985*) and the local reaction field (LRF) long-range treatment of electrostatics. At each site, 20 configurations for the charged and uncharged state were generated. The obtained pK_a values were then converted to free energies for proton translocation.

Additional information

Author contributions

Gordon Williamson, Data curation, Formal analysis, Investigation, Methodology, Writing - review and editing; Giulia Tamburrino, Adriana Bizior, Data curation, Formal analysis, Investigation, Writing - review and editing; Mélanie Boeckstaens, Conceptualization, Data curation, Formal analysis, Methodology, Writing - review and editing; Gaëtan Dias Mirandela, Callum M Ives, Data curation, Formal analysis, Investigation; Marcus G Bage, Formal analysis, Investigation; Andrei Pisliakov, Conceptualization, Formal analysis, Methodology, Writing - review and editing; Eilidh Terras, Investigation; Paul A Hoskisson, Formal analysis, Funding acquisition, Writing - review and editing; Anna Maria Marini, Conceptualization, Methodology, Project administration, Writing - review and editing; Ulrich Zachariae, Conceptualization, Formal analysis, Methodology, Writing - original draft, Project administration; Arnaud Javelle, Conceptualization, Data curation, Formal analysis, Supervision, Investigation, Methodology, Writing - original draft, Project administration

Author ORCIDs

Gordon Williamson (iD) https://orcid.org/0000-0003-3053-8322
Mélanie Boeckstaens (iD) https://orcid.org/0000-0003-1629-7403

Gaëtan Dias Mirandela (iD) https://orcid.org/0000-0001-5871-6288
Andrei Pisliakov (iD) https://orcid.org/0000-0003-1536-0589
Callum M Ives (iD) http://orcid.org/0000-0003-0511-1220
Arnaud Javelle (iD) https://orcid.org/0000-0002-3611-5737

Additional files

Supplementary files

- Supplementary file 1. Supplementary Table 1.

- Transparent reporting form

Data availability

All data generated or analysed during this study are included in the manuscript and supporting files. Source data files have been provided for Figures 1-5 and Table 2. Simulation code is available on GitHub at https://github.com/UZgroup/A-two-lane-mechanism-for-selective-biological-ammonium-transport/ (copy archived at https://github.com/elifesciences-publications/A-two-lane-mechanism-for-selective-biological-ammonium-transport) and the trajectory files are available on Figshare (https://doi.org/10.6084/m9.figshare.12826316).

The following dataset was generated:

Author(s)	Year	Dataset title	Dataset URL	Database and Identifier
Tamburrino G, Zachariae U	2020	Molecular dynamics simulation trajectories, AmtB in twin-His HSD-HSE and HSE-HSD states	https://figshare.com/articles/dataset/Molecular_dynamics_simulation_trajectories_AmtB_in_twin-His_HSD-HSE_and_HSE-HSD_states/12826316	figshare, 10.6084/m9.figshare.12826316

References

Acharya R, Carnevale V, Fiorin G, Levine BG, Polishchuk AL, Balannik V, Samish I, Lamb RA, Pinto LH, DeGrado WF, Klein ML. 2010. Structure and mechanism of proton transport through the transmembrane tetrameric M2 protein bundle of the influenza A virus. *PNAS* **107**:15075–15080. DOI: https://doi.org/10.1073/pnas.1007071107, PMID: 20689043

Andrade SL, Dickmanns A, Ficner R, Einsle O. 2005. Crystal structure of the archaeal ammonium transporter Amt-1 from Archaeoglobus fulgidus. *PNAS* **102**:14994–14999. DOI: https://doi.org/10.1073/pnas.0506254102, PMID: 16214888

Ariz I, Boeckstaens M, Gouveia C, Martins AP, Sanz-Luque E, Fernández E, Soveral G, von Wirén N, Marini AM, Aparicio-Tejo PM, Cruz C. 2018. Nitrogen isotope signature evidences ammonium deprotonation as a common transport mechanism for the AMT-Mep-Rh protein superfamily. *Science Advances* **4**:eaar3599. DOI: https://doi.org/10.1126/sciadv.aar3599, PMID: 30214933

Ashkenazy H, Abadi S, Martz E, Chay O, Mayrose I, Pupko T, Ben-Tal N. 2016. ConSurf 2016: an improved methodology to estimate and visualize evolutionary conservation in macromolecules. *Nucleic Acids Research* **44**:W344–W350. DOI: https://doi.org/10.1093/nar/gkw408, PMID: 27166375

Aydin F, Zhan C, Ritt C, Epsztein R, Elimelech M, Schwegler E, Pham TA. 2020. Similarities and differences between potassium and ammonium ions in liquid water: a first-principles study. *Physical Chemistry Chemical Physics* **22**:2540–2548. DOI: https://doi.org/10.1039/C9CP06163K, PMID: 31942893

Bazzone A, Barthmes M, Fendler K. 2017. SSM-Based electrophysiology for transporter research. *Methods in Enzymology* **594**:31–83. DOI: https://doi.org/10.1016/bs.mie.2017.05.008, PMID: 28779843

Berendsen HJC, Postma JPM, van Gunsteren WF, DiNola A, Haak JR. 1984. Molecular dynamics with coupling to an external bath. *The Journal of Chemical Physics* **81**:3684–3690. DOI: https://doi.org/10.1063/1.448118

Best RB, Zhu X, Shim J, Lopes PE, Mittal J, Feig M, Mackerell AD. 2012. Optimization of the additive CHARMM all-atom protein force field targeting improved sampling of the backbone φ, ψ and side-chain $\chi(1)$ and $\chi(2)$ dihedral angles. *Journal of Chemical Theory and Computation* **8**:3257–3273. DOI: https://doi.org/10.1021/ct300400x, PMID: 23341755

Biver S, Belge H, Bourgeois S, Van Vooren P, Nowik M, Scohy S, Houillier P, Szpirer J, Szpirer C, Wagner CA, Devuyst O, Marini AM. 2008. A role for rhesus factor rhcg in renal ammonium excretion and male fertility. *Nature* **456**:339–343. DOI: https://doi.org/10.1038/nature07518

Boogerd FC, Ma H, Bruggeman FJ, van Heeswijk WC, García-Contreras R, Molenaar D, Krab K, Westerhoff HV. 2011. AmtB-mediated NH3 transport in prokaryotes must be active and as a consequence regulation of transport by GlnK is mandatory to limit futile cycling of NH4(+)/NH3. *FEBS Letters* **585**:23–28. DOI: https://doi.org/10.1016/j.febslet.2010.11.055, PMID: 21134373

Bruce LJ, Guizouarn H, Burton NM, Gabillat N, Poole J, Flatt JF, Brady RL, Borgese F, Delaunay J, Stewart GW. 2009. The monovalent cation leak in overhydrated stomatocytic red blood cells results from amino acid substitutions in the Rh-associated glycoprotein. *Blood* **113**:1350–1357. DOI: https://doi.org/10.1182/blood-2008-07-171140, PMID: 18931342

Bussi G, Donadio D, Parrinello M. 2007. Canonical sampling through velocity rescaling. *The Journal of Chemical Physics* **126**:014101. DOI: https://doi.org/10.1063/1.2408420, PMID: 17212484

Cherif-Zahar B, Durand A, Schmidt I, Hamdaoui N, Matic I, Merrick M, Matassi G. 2007. Evolution and functional characterization of the RH50 gene from the ammonia-oxidizing bacterium *Nitrosomonas europaea*. *Journal of Bacteriology* **189**:9090–9100. DOI: https://doi.org/10.1128/JB.01089-07, PMID: 17921289

Cohen AE, Venkatachalam V. 2014. Bringing bioelectricity to light. *Annual Review of Biophysics* **43**:211–232. DOI: https://doi.org/10.1146/annurev-biophys-051013-022717, PMID: 24773017

Dias Mirandela G, Tamburrino G, Ivanović MT, Strnad FM, Byron O, Rasmussen T, Hoskisson PA, Hub JS, Zachariae U, Gabel F, Javelle A. 2018. Merging In-Solution X-ray and neutron scattering data allows fine structural analysis of Membrane-Protein detergent complexes. *The Journal of Physical Chemistry Letters* **9**: 3910–3914. DOI: https://doi.org/10.1021/acs.jpclett.8b01598, PMID: 29939747

Elbing K, Brent R. 2002. Media preparation and bacteriological tools. *Current Protocols in Molecular Biology* **59**: 1. DOI: https://doi.org/10.1002/0471142727.mb0101s59

Felle H, Porter JS, Slayman CL, Kaback HR. 1980. Quantitative measurements of membrane potential in *Escherichia coli*. *Biochemistry* **19**:3585–3590. DOI: https://doi.org/10.1021/bi00556a026

Ganz P, Ijato T, Porras-Murrilo R, Stührwohldt N, Ludewig U, Neuhäuser B. 2020. A twin histidine motif is the core structure for high-affinity substrate selection in plant ammonium transporters. *Journal of Biological Chemistry* **295**:3362–3370. DOI: https://doi.org/10.1074/jbc.RA119.010891, PMID: 31988244

Gietz D, Jean AS, Woods RA, Schiestl RH. 1992. Improved method for high efficiency transformation of intact yeast cells. *Nucleic Acids Research* **20**:1425. DOI: https://doi.org/10.1093/nar/20.6.1425

Gruswitz F, Chaudhary S, Ho JD, Schlessinger A, Pezeshki B, Ho C-M, Sali A, Westhoff CM, Stroud RM. 2010. Function of human Rh based on structure of RhCG at 2.1 A. *PNAS* **107**:9638–9643. DOI: https://doi.org/10.1073/pnas.1003587107

Hall JA, Yan D. 2013. The molecular basis of K+ exclusion by the *Escherichia coli* ammonium channel AmtB. *The Journal of Biological Chemistry* **288**:14080–14086. DOI: https://doi.org/10.1074/jbc.M113.457952, PMID: 23546877

Hess B, Bekker H, Berendsen HJC, Fraaije JGEM. 1997. LINCS: a linear constraint solver for molecular simulations. *Journal of Computational Chemistry* **18**:1463–1472. DOI: https://doi.org/10.1002/(SICI)1096-987X(199709)18:12<1463::AID-JCC4>3.0.CO;2-H

Hoopen Ft, Cuin TA, Pedas P, Hegelund JN, Shabala S, Schjoerring JK, Jahn TP. 2010. Competition between uptake of ammonium and potassium in barley and Arabidopsis roots: molecular mechanisms and physiological consequences. *Journal of Experimental Botany* **61**:2303–2315. DOI: https://doi.org/10.1093/jxb/erq057

Huang C-H, Ye M. 2010. The Rh protein family: gene evolution, membrane biology, and disease association. *Cellular and Molecular Life Sciences* **67**:1203–1218. DOI: https://doi.org/10.1007/s00018-009-0217-x

Hub JS, de Groot BL, van der Spoel D. 2010a. g_wham—A Free Weighted Histogram Analysis Implementation Including Robust Error and Autocorrelation Estimates. *Journal of Chemical Theory and Computation* **6**:3713–3720. DOI: https://doi.org/10.1021/ct100494z

Hub JS, Winkler FK, Merrick M, de Groot BL. 2010b. Potentials of mean force and permeabilities for carbon dioxide, Ammonia, and water flux across a rhesus protein channel and lipid membranes. *Journal of the American Chemical Society* **132**:13251–13263. DOI: https://doi.org/10.1021/ja102133x, PMID: 20815391

Ishikita H, Knapp EW. 2007. Protonation states of Ammonia/ammonium in the hydrophobic pore of Ammonia transporter protein AmtB. *Journal of the American Chemical Society* **129**:1210–1215. DOI: https://doi.org/10.1021/ja066208n, PMID: 17263403

Jacobs P, Jauniaux J-C, Grenson M. 1980. A cis-dominant regulatory mutation linked to the argB-argC gene cluster in *Saccharomyces cerevisiae*. *Journal of Molecular Biology* **139**:691–704. DOI: https://doi.org/10.1016/0022-2836(80)90055-8

Javelle A, Severi E, Thornton J, Merrick M. 2004. Ammonium sensing in *Escherichia coli*. Role of the ammonium transporter AmtB and AmtB-GlnK complex formation. *The Journal of Biological Chemistry* **279**:8530–8538. DOI: https://doi.org/10.1074/jbc.M312399200, PMID: 14668330

Javelle A, Lupo D, Zheng L, Li XD, Winkler FK, Merrick M. 2006. An unusual twin-his arrangement in the pore of Ammonia channels is essential for substrate conductance. *Journal of Biological Chemistry* **281**:39492–39498. DOI: https://doi.org/10.1074/jbc.M608325200, PMID: 17040913

Jorgensen WL, Chandrasekhar J, Madura JD, Impey RW, Klein ML. 1983. Comparison of simple potential functions for simulating liquid water. *The Journal of Chemical Physics* **79**:926–935. DOI: https://doi.org/10.1063/1.445869

Kato M, Pisliakov AV, Warshel A. 2006. The barrier for proton transport in aquaporins as a challenge for electrostatic models: The role of protein relaxation in mutational calculations. *Proteins: Structure, Function, and Bioinformatics* **64**:829–844. DOI: https://doi.org/10.1002/prot.21012

Khademi S, O'Connell J, Remis J, Robles-Colmenares Y, Miercke LJ, Stroud RM. 2004. Mechanism of Ammonia transport by amt/MEP/Rh: structure of AmtB at 1.35 A. *Science* **305**:1587–1594. DOI: https://doi.org/10.1126/science.1101952, PMID: 15361618

Kopec W, Köpfer DA, Vickery ON, Bondarenko AS, Jansen TLC, de Groot BL, Zachariae U. 2018. Direct knock-on of desolvated ions governs strict ion selectivity in K$^+$ channels. *Nature Chemistry* **10**:813–820. DOI: https://doi.org/10.1038/s41557-018-0105-9

Kutzner C, Köpfer DA, Machtens JP, de Groot BL, Song C, Zachariae U. 2016. Insights into the function of ion channels by computational electrophysiology simulations. *Biochimica Et Biophysica Acta (BBA) - Biomembranes* **1858**:1741–1752. DOI: https://doi.org/10.1016/j.bbamem.2016.02.006, PMID: 26874204

Lamoureux G, Klein ML, Bernèche S. 2007. A stable water chain in the hydrophobic pore of the AmtB ammonium transporter. *Biophysical Journal* **92**:L82–L84. DOI: https://doi.org/10.1529/biophysj.106.102756, PMID: 17351012

Lee FS, Chu ZT, Warshel A. 1993. Microscopic and semimicroscopic calculations of electrostatic energies in proteins by the POLARIS and ENZYMIX programs. *Journal of Computational Chemistry* **14**:161–185. DOI: https://doi.org/10.1002/jcc.540140205

Lee J, Cheng X, Swails JM, Yeom MS, Eastman PK, Lemkul JA, Wei S, Buckner J, Jeong JC, Qi Y, Jo S, Pande VS, Case DA, Brooks CL, MacKerell AD, Klauda JB, Im W. 2016. CHARMM-GUI input generator for NAMD, GROMACS, AMBER, OpenMM, and CHARMM/OpenMM simulations using the CHARMM36 additive force field. *Journal of Chemical Theory and Computation* **12**:405–413. DOI: https://doi.org/10.1021/acs.jctc.5b00935, PMID: 26631602

Li X, Jayachandran S, Nguyen H-HT, Chan MK. 2007. Structure of the *Nitrosomonas europaea* Rh protein. *PNAS* **104**:19279–19284. DOI: https://doi.org/10.1073/pnas.0709710104

Ludewig U, von Wirén N, Frommer WB. 2002. Uniport of NH4+ by the root hair plasma membrane ammonium transporter LeAMT1;1. *Journal of Biological Chemistry* **277**:13548–13555. DOI: https://doi.org/10.1074/jbc.M200739200, PMID: 11821433

Lupo D, Li X-D, Durand A, Tomizaki T, Cherif-Zahar B, Matassi G, Merrick M, Winkler FK. 2007. The 1.3-A resolution structure of *Nitrosomonas europaea* Rh50 and mechanistic implications for NH3 transport by Rhesus family proteins. *PNAS* **104**:19303–19308. DOI: https://doi.org/10.1073/pnas.0706563104

Maeda K, Westerhoff HV, Kurata H, Boogerd FC. 2019. Ranking network mechanisms by how they fit diverse experiments and deciding on *E. coli*'s ammonium transport and assimilation network. *Npj Systems Biology and Applications* **5**:14. DOI: https://doi.org/10.1038/s41540-019-0091-6, PMID: 30993002

Marini AM, Soussi-Boudekou S, Vissers S, Andre B. 1997. A family of ammonium transporters in *Saccharomyces cerevisiae*. *Molecular and Cellular Biology* **17**:4282–4293. DOI: https://doi.org/10.1128/MCB.17.8.4282

Marini AM, Boeckstaens M, Benjelloun F, Chérif-Zahar B, André B. 2006. Structural involvement in substrate recognition of an essential aspartate residue conserved in Mep/Amt and Rh-type ammonium transporters. *Current Genetics* **49**:364–374. DOI: https://doi.org/10.1007/s00294-006-0062-5

Mayer M, Dynowski M, Ludewig U. 2006. Ammonium ion transport by the AMT/Rh homologue LeAMT1;1. *Biochemical Journal* **396**:431–437. DOI: https://doi.org/10.1042/BJ20060051

McDonald TR, Ward JM. 2016. Evolution of electrogenic ammonium transporters (AMTs). *Frontiers in Plant Science* **7**:352. DOI: https://doi.org/10.3389/fpls.2016.00352, PMID: 27066024

Mirandela GD, Tamburrino G, Hoskisson PA, Zachariae U, Javelle A. 2019. The lipid environment determines the activity of the *Escherichia coli* ammonium transporter AmtB. *The FASEB Journal* **33**:1989–1999. DOI: https://doi.org/10.1096/fj.201800782R, PMID: 30211659

Miroux B, Walker JE. 1996. Over-production of proteins *in Escherichia coli*: mutant hosts that allow synthesis of some membrane proteins and globular proteins at high levels. *Journal of Molecular Biology* **260**:289–298. DOI: https://doi.org/10.1006/jmbi.1996.0399, PMID: 8757792

Miyamoto S, Kollman PA. 1992. Settle: An analytical version of the SHAKE and RATTLE algorithm for rigid water models. *Journal of Computational Chemistry* **13**:952–962. DOI: https://doi.org/10.1002/jcc.540130805

Mumberg D, Muller R, Funk M. 1994. Regulatable promoters of *Saccharomyces cerevisiae*: comparison of transcriptional activity and their use for heterologous expression. *Nucleic Acids Research* **22**:5767–5768. DOI: https://doi.org/10.1093/nar/22.25.5767

Neuhäuser B, Dynowski M, Ludewig U. 2014. Switching substrate specificity of AMT/MEP/ Rh proteins. *Channels* **8**:496–502. DOI: https://doi.org/10.4161/19336950.2014.967618, PMID: 25483282

Nygaard TP, Rovira C, Peters GH, Jensen MØ. 2006. Ammonium recruitment and Ammonia transport by *E. coli* Ammonia channel AmtB. *Biophysical Journal* **91**:4401–4412. DOI: https://doi.org/10.1529/biophysj.106.089714, PMID: 17012311

Rentsch D, Laloi M, Rouhara I, Schmelzer E, Delrot S, Frommer WB. 1995. *NTR1* encodes a high affinity oligopeptide transporter in *Arabidopsis*. *FEBS Letters* **370**:264–268. DOI: https://doi.org/10.1016/0014-5793(95)00853-2

Sham YY, Chu ZT, Tao H, Warshel A. 2000. Examining methods for calculations of binding free energies: lra, LIE, PDLD-LRA, and PDLD/S-LRA calculations of ligands binding to an HIV protease. *Proteins: Structure, Function, and Genetics* **39**:393–407. DOI: https://doi.org/10.1002/(SICI)1097-0134(20000601)39:4<393::AID-PROT120>3.0.CO;2-H, PMID: 10813821

Smart OS, Neduvelil JG, Wang X, Wallace BA, Sansom MSP. 1996. HOLE: A program for the analysis of the pore dimensions of ion channel structural models. *Journal of Molecular Graphics* **14**:354–360. DOI: https://doi.org/10.1016/S0263-7855(97)00009-X

Thomas GH, Mullins JGL, Merrick M. 2000. Membrane topology of the Mep/Amt family of ammonium transporters. *Molecular Microbiology* **37**:331–344. DOI: https://doi.org/10.1046/j.1365-2958.2000.01994.x

Torrie GM, Valleau JP. 1977. Nonphysical sampling distributions in Monte Carlo free-energy estimation: Umbrella sampling. *Journal of Computational Physics* **23**:187–199. DOI: https://doi.org/10.1016/0021-9991(77)90121-8

van den Berg B, Chembath A, Jefferies D, Basle A, Khalid S, Rutherford JC. 2016. Structural basis for Mep2 ammonium transceptor activation by phosphorylation. *Nature Communications* **7**:11337. DOI: https://doi.org/10.1038/ncomms11337

Wacker T, Garcia-Celma JJ, Lewe P, Andrade SLA. 2014. Direct observation of electrogenic NH_4^+ transport in ammonium transport (Amt) proteins. *PNAS* **111**:9995–10000. DOI: https://doi.org/10.1073/pnas.1406409111

Wang S, Orabi EA, Baday S, Bernèche S, Lamoureux G. 2012. Ammonium transporters achieve charge transfer by fragmenting their substrate. *Journal of the American Chemical Society* **134**:10419–10427. DOI: https://doi.org/10.1021/ja300129x, PMID: 22631217

Warshel A, King G. 1985. Polarization constraints in molecular dynamics simulation of aqueous solutions: The surface constraint all atom solvent (SCAAS) model. *Chemical Physics Letters* **121**:124–129. DOI: https://doi.org/10.1016/0009-2614(85)87168-2

Weidinger K, Neuhäuser B, Gilch S, Ludewig U, Meyer O, Schmidt I. 2007. Functional and physiological evidence for a rhesus-type Ammonia transporter in *Nitrosomonas europaea*. *FEMS Microbiology Letters* **273**:260–267. DOI: https://doi.org/10.1111/j.1574-6968.2007.00805.x, PMID: 17608700

Wiechert M, Beitz E. 2017. Mechanism of formate-nitrite transporters by dielectric shift of substrate acidity. *The EMBO Journal* **36**:949–958. DOI: https://doi.org/10.15252/embj.201695776, PMID: 28250043

Zheng L, Kostrewa D, Berneche S, Winkler FK, Li X-D. 2004. The mechanism of ammonia transport based on the crystal structure of AmtB of *Escherichia coli*. *PNAS* **101**:17090–17095. DOI: https://doi.org/10.1073/pnas.0406475101